Gravitational waves from vacuum first-order phase transitions : From the envelope to the lattice

Cutting, Daniel

2018-06-12

Gravitational waves from vacuum first-order phase transitions: From the envelope to the lattice

Daniel Cutting,[1,2,*] Mark Hindmarsh,[2,†] and David J. Weir[2,‡]

[1]*Department of Physics and Astronomy, University of Sussex,*
Falmer, Brighton BN1 9QH, United Kingdom
[2]*Department of Physics and Helsinki Institute of Physics,*
P.O. Box 64, FI-00014 University of Helsinki, Finland

We conduct large scale numerical simulations of gravitational wave production at a first-order vacuum phase transition. We find a power law for the gravitational wave power spectrum at high wave number which falls off as $k^{-1.5}$ rather than the k^{-1} produced by the envelope approximation. The peak of the power spectrum is shifted to slightly lower wave numbers from that of the envelope approximation. The envelope approximation reproduces our results for the peak power less well, agreeing only to within an order of magnitude. After the bubbles finish colliding, the scalar field oscillates around the true vacuum. An additional feature is produced in the UV of the gravitational wave power spectrum, and this continues to grow linearly until the end of our simulation. The additional feature peaks at a length scale close to the bubble wall thickness and is shown to have a negligible contribution to the energy in gravitational waves, providing the scalar field mass is much smaller than the Planck mass.

I. INTRODUCTION

The first direct detection of gravitational waves [1,2] has brought in a new era of gravitational wave astronomy. Future space based gravitational wave observatories such as LISA [3] hold great promise for cosmology [4]. LISA's planned sensitivity band peaks at lower frequencies than ground based detectors. It therefore will have much greater sensitivity to gravitational waves originating from process in the very early Universe. Cosmological first-order phase transitions are one such process, and LISA's sensitivity window allows it to probe electroweak phase transitions in many extensions of the Standard Model [5,6].

In a cosmological first-order phase transition, the Universe changes from a metastable high energy (symmetric) phase to a stable lower energy (broken) phase. This occurs through the quantum or thermal nucleation of bubbles of the broken phase [7–9], separated from the surrounding unbroken phase by a thin wall. These bubbles then expand, collide and eventually coalesce. This process generates shear stresses which in turn source gravitational waves [10,11].

Early work focused on characterizing the signal from a phase transition that occurs in vacuum [12]. In such a transition, the bubble wall quickly accelerates to ultra-relativistic velocities.

A model of such a scenario was developed, termed the envelope approximation [13]. In this model, the shear stresses are assumed to be concentrated in an infinitesimally thin shell located at the bubble wall. Upon the collision of the bubble walls, the shear stress is assumed to dissipate, and so any regions where bubbles overlap are ignored. The characteristic gravitational wave power spectrum from the envelope approximation is a broken power law in wave number k, where the spectrum rises as k^3 from the low-wave-number (IR) direction and falls off as k^{-1} in the high-wave-number (UV) direction. The peak of the broken power law is associated with the length scale of the average bubble separation R_*.

Although the envelope approximation was originally created for bubbles expanding in vacuum it was quickly applied to thermal first-order phase transitions, in which the scalar bubbles expand in a hot plasma [14–16]. In this case, frictional effects from the plasma typically cause the bubble wall to approach a terminal speed v_w. which is not generally ultrarelativistic. Then the majority of the energy liberated from the phase transition is deposited into heat or the bulk motion of the plasma, and the gravitational waves sourced from the shear stress in the scalar field are negligible. It was argued that, providing the shear stress in the plasma is assumed to be in an infinitesimally thin envelope at the bubble wall, the envelope approximation can once again be applied [14]. Later modeling of bubble

*d.cutting@sussex.ac.uk
†m.b.hindmarsh@sussex.ac.uk
‡david.weir@helsinki.fi

collisions introduced a thick fluid shell, and proposed that the velocity field should be Gaussian [17].

Large scale three-dimensional hydrodynamical simulations [18–20] have dramatically changed the picture. They show that the shear stresses do not disappear with the bubbles, and persist for long after the transition completes, in the form of sound waves. The envelope approximation is not a good description of total gravitational wave production, and predicts incorrectly both the amplitude and shape of the gravitational wave power spectrum. A better picture of the postcollision phase is one of many overlapping counterpropagating sound shells [21].

On the other hand, the envelope approximation does correctly describe the sub-dominant contribution to the power spectrum from the scalar field [22], and analytic studies within the envelope approximation have confirmed the broken power laws found from numerical simulations [23]. The envelope approximation can also accommodate the idea that fluid shells persist after collision [16,24].

It is therefore widely believed that the envelope approximation describes the gravitational power in cases where the energy-momentum of the system is dominated by the scalar field, where the system is close to its vacuum state. In this paper, we investigate the quality of the envelope approximation with three-dimensional numerical simulations of a first-order vacuum phase transition.

Classical lattice simulations of a vacuum phase transition have been used to study the power spectrum produced from bubble collisions before [12,25]. A one-dimensional simulation of the collision of two scalar field bubbles was carried out in Ref. [12]. and used to motivate the envelope approximation in Ref. [26].

In Ref. [25], it was claimed that the power spectrum produced from collisions in three-dimensional simulations with several bubbles was several orders of magnitude smaller than that predicted by the envelope approximation. Furthermore, after the bubbles had finished colliding there appeared to be an additional phase of the transition in which the scalar field continued to oscillate around the true vacuum. During this oscillation phase the power spectrum continued to grow and the peak of the spectrum shifted towards a higher frequency.

Our numerical simulations adopt similar techniques. However, we are able to perform simulations with many more bubbles and higher wall velocities than Ref. [25].

The simulations solve the field equations for a scalar field sourcing gravitational waves in the linear approximation. The transition is modeled by introducing bubbles of the broken phase as initial conditions for the scalar field. This is done in three different ways, modeling three different histories of bubble nucleation. In simultaneous nucleation, we introduce all bubbles at the very start of the simulation. In exponential nucleation simulations, we introduce the bubbles with an exponentially increasing rate per unit volume. In constant nucleation, we introduce the bubbles at a constant rate.

We show power spectra for both the scalar field itself and also the resulting gravitational wave power spectrum for all nucleation types. We find that as we increase the wall velocity to ultrarelativistic speeds, the slope of the gravitational wave power spectrum towards the UV becomes steeper than k^{-1}, and approaches $k^{-1.5}$. The peak amplitude and peak location are similar to those predicted by the envelope approximation. We provide a fit for the power spectrum generated from bubble collisions.

We also confirm the existence of a phase after the bubble collisions have finished, during which the scalar field oscillates around the true vacuum and continues to source gravitational waves. This creates an additional bump in the power spectrum that is associated with the mass scale of the scalar field. This continues to grow linearly until very late times, but we show that it has a negligible contribution to the power spectrum in comparison that of bubble collisions, providing that the mass of the scalar field is smaller than the Planck mass.

In the following section, we recap the dynamics of the scalar field during a vacuum phase transition. This includes the physics of the scalar field during bubble nucleation, expansion, and the eventual collision and oscillation phases of the transition. In Sec. III, we describe how the scalar field sources gravitational waves, and also describe the envelope approximation. The numerical methods used to perform our simulations are discussed in Sec. IV. Our results are split into two parts; in Sec. V, we present the behavior of the scalar field within our simulations, and in Sec. VI, we analyze the gravitational wave power spectra from our simulations and compare them to the envelope approximation. Our conclusions are listed in Sec. VII.

II. DYNAMICS OF VACUUM TRANSITIONS

A. Scalar field dynamics

In a first-order vacuum transition, bubbles of a new phase of a scalar field nucleate and then expand at ultrarelativistic speeds. At the interface between the two phases a bubble wall forms. In this region, the scalar field varies smoothly between the two vacuum expectation values. Upon the collision and subsequently merger of the bubbles the shear stress of the system will source gravitational waves. The shear stress in a vacuum transition is predominantly due to gradients in the scalar field ϕ.

In this work, we study transitions in which the duration of the phase transition is much shorter than the Hubble time H_*^{-1} when the transition takes place. For such transitions, the expansion of the Universe can be neglected, and the equation of motion for the scalar field is simply given by

$$\Box\phi - V'(\phi) = 0, \tag{1}$$

where $V(\phi)$ is the effective potential of the scalar field. This is sufficient to investigate the envelope approximation, but may not give accurate results for transitions in which the Universe enters an inflationary phase before bubbles start nucleating.

For these purposes it is sufficient to adopt a simple quartic form for the effective potential,

$$V(\phi) = \frac{1}{2}M^2\phi^2 + \frac{1}{3}\delta\phi^3 + \frac{1}{4}\lambda\phi^4, \qquad (2)$$

where the presence of a cubic term allows us to ensure the transition is first order. The value of the scalar field in the broken phase is then

$$\phi_b = \frac{-\delta + \sqrt{\delta^2 - 4M^2\lambda}}{2\lambda}, \qquad (3)$$

with mass

$$M_b = \sqrt{-\delta\phi_b - 2M^2}, \qquad (4)$$

The potential difference between the two minima is given by

$$\rho_{vac} = \frac{1}{12\lambda}(M_b^4 - M^4). \qquad (5)$$

By varying the couplings M^2, δ and λ we are able to change the potential difference ρ_{vac} between the two minima of our potential, and also the height of the potential barrier.

The total energy density in the scalar field ρ_ϕ can be split into three components,

$$\rho_\phi = \rho_K + \rho_V + \rho_D, \qquad (6)$$

with the kinetic energy density,

$$\rho_K = \frac{1}{2}\dot{\phi}^2, \qquad (7)$$

the gradient energy density,

$$\rho_D = \frac{1}{2}(\nabla\phi)^2, \qquad (8)$$

and the potential energy density,

$$\rho_V = V(\phi) - V(\phi_b). \qquad (9)$$

B. Bubble nucleation

In a first-order vacuum transition, bubbles nucleate by quantum tunneling through a potential barrier. This means that they nucleate as critical bubbles, O(4)-symmetric solutions to the Euclidean field equations [7,8]. When the radius of the critical bubble is much larger than the thickness of the bubble wall the bubble is said to be in the thin wall limit. This occurs when ρ_{vac} is much smaller than the height of the potential barrier, or equivalently when the minima are close to degenerate. For our potential the minima are degenerate for

$$\delta = -\frac{3}{\sqrt{2}}M\sqrt{\lambda}. \qquad (10)$$

When ρ_{vac} is much larger than the height of the potential barrier, the critical bubble is of a similar size to the radius. We leave the study of such bubbles to a later work.

The thin wall solution can be calculated analytically as a function of Euclidean radius, $r_E = \sqrt{r^2 + \tau^2}$, where r is the spatial radius, and τ the Euclidean time. In the thin wall limit, the scalar field profile of the critical bubble is given by

$$\phi_c(r) = \frac{\phi_b}{2}\left[1 - \tanh\left(\frac{r - R_c^{tw}}{l_0^{tw}}\right)\right], \qquad (11)$$

where l_0 is thickness of the bubble wall, which is given in the thin wall limit by

$$l_0^{tw} = \frac{2}{\sqrt{V''(\phi_b)}}, \qquad (12)$$

and R_c^{tw} is the radius of the critical bubble. The radius of the critical bubble can be estimated by extremizing the approximate expression for the Euclidean action

$$S_4 = 2\pi^2 R^3\sigma^{tw} - \frac{\pi^2}{2}R^4\rho_{vac}, \qquad (13)$$

where

$$\sigma^{tw} = \frac{M^3}{3\lambda}, \qquad (14)$$

is interpreted as the surface tension of the bubble. Then the critical radius is

$$R_c^{tw} = \frac{3\sigma^{tw}}{\rho_{vac}}. \qquad (15)$$

At the point of time symmetry $\tau = 0$, the energy liberated from the vacuum is equal to the energy in the wall. Furthermore, the outward force on the bubble wall due to the pressure difference ρ_{vac} is equal and opposite to that caused by the surface tension.

Once the bubble has nucleated, the solution is found by the analytic continuation to Minkowski space, so that

$$\phi(r,t) = \begin{cases} \phi_c(\sqrt{r^2 - t^2}), & r > t, \\ \phi_b, & r \le t. \end{cases} \qquad (16)$$

The probability of nucleating a bubble per unit volume per unit time $p(t)$ is given by [8]

$$p(t) = p_n \exp(-S_4). \qquad (17)$$

Very often the Euclidean action decreases slowly in time due to a change in temperature or a background field. Then we may write

$$p(t) = p_f \exp[\beta(t - t_f)], \qquad (18)$$

where $\beta = -d \ln p(t)/dt|_{t_f}$ and t_f is the time at which the fraction of the Universe in the symmetric phase is $h(t_f) = 1/e$ [27]. The bubble number density can be shown to be

$$n_b = \frac{1}{8\pi} \frac{\beta^3}{v_w^3}, \qquad (19)$$

where in the vacuum case v_w is very close to unity. We will refer to this case as exponential nucleation.

It is also possible that $S_4(t)$ has a minimum which is reached at time t_0 before a transition completes. Then the probability of nucleating a bubble per unit volume could be approximated by

$$p(t) = p_0 \exp\left[-\frac{1}{2}\beta_2^2(t - t_0)^2\right], \qquad (20)$$

where $\beta_2 = \sqrt{S''(t_0)}$. Nucleation is then concentrated around time t_0 [28]. The bubble density is

$$n_b = \sqrt{2\pi}\frac{p_0}{\beta_2}. \qquad (21)$$

We will refer to this case as simultaneous nucleation.

The last possibility we consider is if $S_4(t)$ tends to a constant (for a model with a constant nucleation rate see Ref. [29]). We would then expect bubbles to nucleate at a constant rate

$$p(t) = p_c, \qquad (22)$$

for which

$$n_b = \frac{1}{4}\left(\frac{3}{\pi}\right)^{1/4}\Gamma\left(\frac{1}{4}\right)\left(\frac{p_c}{v_w}\right)^{3/4}. \qquad (23)$$

We will refer to this as constant nucleation.

C. Bubble growth

If we consider a thin wall bubble then we can obtain an expression for the evolution of the bubble simply by considering energy conservation. The energy in the static bubble wall per unit area is simply σ^{tw}. Then if the bubble wall is expanding at some velocity v_w, the energy per unit area is given by $\sigma^{tw}\gamma$ where γ is the wall's Lorentz factor. The total energy of an expanding bubble with radius R is then [7,8]

$$E_{bub} = 4\pi R^2 \sigma^{tw}\gamma - \frac{4}{3}\pi R^3 \rho_{vac}, \qquad (24)$$

where we can define R to be the point in the scalar field profile such that $\phi(R) = \phi_b/2$. As we are considering vacuum decay, we expect $E_{bub} = 0$. We therefore obtain that, for a bubble of radius R, the Lorentz factor of the bubble wall is given by

$$\gamma(R) = \frac{R\rho_{vac}}{3\sigma^{tw}} = \frac{R}{R_c^{tw}}. \qquad (25)$$

We expect Eq. (25) to apply outside the thin wall limit by recalling that the solution of the classical field equations is simply the analytic continuation of the O(4)-symmetric bounce solution [7]. Then any point in the field profile of the critical bubble we define to be the critical radius R_c will expand out with a hyperboloid motion satisfying

$$R^2(t) - t^2 = R_c^2, \qquad (26)$$

which is equivalent to Eq. (25).

D. Bubble collision and oscillation phase

For bubbles with thin walls, after collision part of the overlap region rebounds and returns towards the false vacuum [30,31]. In Fig. 1, we plot the variation during a collision of the scalar field along the collision axis connecting two bubble centers. At the collision point it can be seen that the scalar field oscillates between the true and false vacuum. These large amplitude oscillations are the source of scalar radiation moving at close to the speed of
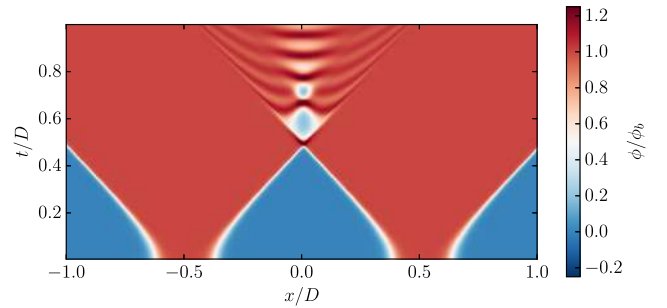

FIG. 1. Values of the scalar field along the collision axis during a two bubble collision where $R_c M = 7.15$. Here the x axis is the collision axis which connects the two bubble centers. The y axis is time since the nucleation of the bubbles. The bubbles are separated by a distance D. This figure can be compared with Fig. 1 of [30] and Fig. 7 of [31].

light, and can also induce rapid production of light particles through parametric resonance [32]. This rebounding and oscillation phase is something that is not accounted for within the envelope approximation. Away from the thin wall limit, the scalar field in the overlap region is not able to return to the false vacuum, and instead will just oscillate around the true vacuum [31].

After this stage, the scalar field continues to oscillate around the true vacuum with large amplitude oscillations. In the absence of other interactions, scalar fields take a substantial time to thermalize [33–35].

III. GRAVITATIONAL WAVES FROM A PHASE TRANSITION

In order to calculate the gravitational wave power spectrum, we need to find the transverse traceless (TT) metric perturbations h_{ij}^{TT} where

$$\Box h_{ij}^{\mathrm{TT}} = 16\pi G T_{ij}^{\mathrm{TT}}, \qquad (27)$$

and T_{ij}^{TT} is the transverse traceless projection of the energy-momentum tensor,

$$T_{\mu\nu} = \partial_\mu \phi \partial_\nu \phi - \eta_{\mu\nu}\left(\frac{1}{2}(\partial\phi)^2 + V(\phi)\right), \qquad (28)$$

where $\eta_{\mu\nu}$ is the Minkowski metric. The energy density in the gravitational waves can be defined as

$$\rho_{\mathrm{gw}}(\mathbf{x}, t) = \frac{1}{32\pi G}\dot{h}_{ij}^{\mathrm{TT}}\dot{h}_{ij}^{\mathrm{TT}}. \qquad (29)$$

Note that an average over many wavelengths and periods may be needed in order to reduce fluctuations in this quantity.

We introduce an auxiliary tensor u_{ij} which satisfies [36]

$$\Box u_{ij} = 16\pi G(\partial_i\phi)(\partial_j\phi). \qquad (30)$$

To obtain h_{ij}^{TT} we use the projector $\Lambda_{ij,lm}$ on u_{ij} in momentum space,

$$h_{ij}^{\mathrm{TT}}(\mathbf{k}, t) = \Lambda_{ij,lm}(\mathbf{k})u_{lm}(\mathbf{k}, t), \qquad (31)$$

where

$$\Lambda_{ij,lm}(\mathbf{k}) = P_{im}(\mathbf{k})P_{jl}(\mathbf{k}) - \frac{1}{2}P_{ij}(\mathbf{k})P_{lm}(\mathbf{k}), \qquad (32)$$

and

$$P_{ij}(\mathbf{k}) = \delta_{ij} - \hat{k}_i\hat{k}_j. \qquad (33)$$

We then define the spectral density of the time derivative of the metric perturbations $P_{\dot{h}}$ as

$$\langle \dot{h}_{ij}^{\mathrm{TT}}(\mathbf{k}, t)\dot{h}_{ij}^{\mathrm{TT}}(\mathbf{k}', t)\rangle = P_{\dot{h}}(\mathbf{k}, t)(2\pi)^3\delta(\mathbf{k} + \mathbf{k}'). \qquad (34)$$

Therefore the power spectrum of gravitational wave energy density is

$$\frac{d\rho_{\mathrm{gw}}}{d\ln(k)} = \frac{1}{32\pi G}\frac{k^3}{2\pi^2}P_{\dot{h}}(\mathbf{k}, t), \qquad (35)$$

and by dividing through by the critical energy density ρ_c we obtain the power spectrum of the gravitational wave energy density parameter

$$\frac{d\Omega_{\mathrm{gw}}}{d\ln(k)} = \frac{1}{32\pi G\rho_c}\frac{k^3}{2\pi^2}P_{\dot{h}}(\mathbf{k}, t). \qquad (36)$$

A. Collision phase: Envelope approximation

In the envelope approximation [13], the bubble walls are treated as infinitely thin, expanding with speed v_{w}, and containing all the vacuum energy released by the transition. The overlap region of collided bubbles are ignored, and the gravitational waves from shear stress "envelope" calculated. The resulting spectrum was re-computed with many more bubbles in Ref. [15], and again in Ref. [16], for an exponential nucleation rate in both cases.

The gravitational wave power spectrum is well approximated by a broken power law

$$\frac{d\Omega_{\mathrm{gw}}^{\mathrm{env}}}{d\ln(k)} = \Omega_{\mathrm{p}}^{\mathrm{env}}\frac{(a+b)\tilde{k}^b k^a}{b\tilde{k}^{(a+b)} + ak^{(a+b)}}, \qquad (37)$$

with power law exponents a and b, peak amplitude $\Omega_{\mathrm{p}}^{\mathrm{env}}$ and peak wave number $\tilde{k}$. The peak amplitude was found to be

$$\Omega_{\mathrm{p}}^{\mathrm{env}} \simeq \frac{0.44v_w^3}{1 + 8.28v_w^3}\left(\frac{H_*}{\beta}\right)^2(\kappa_\phi\Omega_{\mathrm{vac}})^2, \qquad (38)$$

where the Hubble rate at the time of the transition H_*, the vacuum energy density parameter $\Omega_{\mathrm{vac}} = \rho_{\mathrm{vac}}/\rho_c$ and the bubble wall velocity v_{w}. The peak frequency was estimated to be

$$\tilde{k}/\beta \simeq \frac{1.96}{1 - 0.051v_{\mathrm{w}} + 0.88v_{\mathrm{w}}^2}. \qquad (39)$$

The efficiency factor κ_ϕ measures the fraction of vacuum energy that is converted to stress energy localized at the bubble wall. We define it as

$$\kappa_\phi = \frac{2\rho_D}{\rho_{\mathrm{vac}} - \rho_{\mathrm{V}}}. \qquad (40)$$

For a vacuum phase transition $\kappa_\phi \simeq 1$.

The exponent for the broken power law on the low frequency side is expected to be $a = 3$ due to causality [37]. In Ref. [16], the power law exponents were found to be $a = 2.9$ and $b = 0.9$ for $v_w \simeq 1$ and $a = 2.95$ and $b = 1$ for $v_w \ll 1$. Furthermore, in Ref. [22], the envelope approximation was compared to lattice simulations of a scalar field with frictional effects chosen such that the bubble walls asymptotes a constant speed $v_w = 0.44$. The gravitational wave power spectrum generated by stress energy in the scalar field was found to agree well with the envelope approximation. The power law exponents for the envelope approximation in this study were found to be $a = 2.98 \pm 0.02$ and $b = 0.62 \pm 0.05$ [22].

There is also some analytical understanding of the power spectrum produced under the envelope approximation. In Ref. [23], it is shown that the two point correlator of the energy-momentum tensor can be expressed as a one-dimensional integral under the envelope approximation, also producing a broken power law with exponents $a = 3$ and $b = 1$.

It should be noted that while typically in a thermal phase transition friction effects from the plasma cause v_w to approach a constant, in a vacuum phase transition the bubble wall accelerates until collision with $v_w \to 1$ and $\gamma \to \infty$. In this current work, we shall check whether the formula is a good fit in the case where the bubble wall continues to accelerate until collision, reaching ultrarelativistic velocities.

B. Oscillation phase

Previous simulations of a vacuum first-order phase transition have observed that after all the bubble collisions have completed, the scalar field continues to oscillate, and the production of gravitational radiation continues [25].

The contribution to the gravitational wave power spectrum from this oscillation phase was seen to dominate that of the bubble collisions by more than an order of magnitude. The peak frequency moved towards the UV by an order of magnitude during the oscillation phase.

Providing the oscillations in the scalar field are nonlinear [38] we would expect them to be a continuous source of gravitational waves, similar to acoustic waves in a thermal phase transition [19]. Eventually Hubble friction would damp out the oscillations.

A further goal of the current work is to investigate if we also see the growth of the gravitational wave power spectrum during an oscillation phase in our simulations.

IV. METHODS

To perform our study we perform a series of simulations solving the partial differential equations (1) and (30) on a three-dimensional lattice, using code built on the open source C++ library LATfield2 [39]. To compute derivatives we use a central finite difference method. For the Laplacian

TABLE I. Critical radii R_c and wall thicknesses l_0 that are used in our simulations. For each of these we give the potential parameters δ and λ used to derive them, the broken phase value of the scalar field ϕ_b and the vacuum energy density ρ_{vac}. We also list the surface tension σ^{tw}, wall thickness l_0^{tw} and critical radius R_c^{tw} as derived from the thin wall approximation.

$R_c M$	$l_0 M$	δ/M	λ	ϕ_b/M	ρ_{vac}/M^4	σ^{tw}/M^3	$l_0^{tw} M$	$R_c^{tw} M$
7.15	1.71	−1.632	0.5	2.45	0.495	2/3	1.42	4.04
14.3	1.83	−1.56	0.5	2.22	0.189	2/3	1.65	10.6
28.8	1.91	−1.528	0.5	2.11	0.0809	2/3	1.81	24.7

we use the minimal 7-point stencil made up of a central point and then an additional 2 points in each dimension. We choose our timestep Δt and lattice spacing Δx such that $\Delta t = 0.2 \Delta x$. We advance in timestep by using the leapfrog algorithm.

Our simulations are on a cubic grid with total volume $\mathcal{V} = (L \Delta x)^3$, and periodic boundary conditions. We begin each simulation by nucleating at least one bubble at the simulation time $t = 0$. The total number of bubbles nucleated by the end of the simulation is given by N_b.

We use a shooting method to find the critical profile for specific values of M^2, δ and λ. We choose three profiles to simulate and give the parameters for these in Table I. The resulting field profiles are modeled well by Eq. (11) with values for R_c and l_0 given in the first two columns. Note that they differ from the thin wall values due to the finite size of the bubble.

The value of R_c is given by the location in the numerical profile at which

$$\phi_c(R_c) = \frac{\phi_b}{2}. \tag{41}$$

Similarly, $l_0 = r^+ - r^-$ where

$$\phi_c(r^\pm) = \frac{\phi_b}{2}(1 - \tanh(\pm 1/2)). \tag{42}$$

We nucleate bubbles with a critical profile inside our numerical simulation. Before nucleating the Nth bubble, we check that, for all $n < N$, the distance between the Nth and nth bubble centers r_n obeys the following relation

$$r_n^{sep} > R_c + \sqrt{R_c^2 + (t - t_n)^2}, \tag{43}$$

where t_n is the time at which the nth bubble nucleated. Providing this is satisfied for all bubbles, we nucleate a bubble by modifying $\phi \to \phi'$, where

$$\phi'(r) = \sqrt{\phi^2(r) + \phi_c^2(r)}. \tag{44}$$

We evolve the auxiliary metric tensor u_{ij} in real space at every timestep. At routine intervals we perform a Fourier

TABLE II. Parameters of the simultaneous nucleation simulations used within this paper. Listed here for each run is the critical radius R_c, typical Lorentz factor at collision γ_*, average bubble seperation R_*, number of bubbles N_b, number of lattice points L^3, lattice spacing Δx, and effective γ_* as found on the lattice γ_*^{lat}. Not given here are simulation runs where the metric perturbations are turned on after the bubbles have finished colliding, see Table V.

$R_c M$	γ_*	$R_* M$	N_b	$L\Delta x M$	L	$\Delta x M$	γ_*^{lat}
7.15	1.97	28.2	8	56.32	128	0.44	1.85
7.15	1.97	28.2	64	112.64	256	0.44	1.85
7.15	1.97	28.2	512	225.28	512	0.44	1.85
7.15	1.97	28.2	4096	450.56	1024	0.44	1.85
7.15	3.94	56.3	8	112.64	512	0.22	3.37
7.15	3.94	56.3	64	225.28	1024	0.22	3.37
7.15	3.94	56.3	512	450.56	2048	0.22	3.37
7.15	3.94	56.3	4096	901.12	4096	0.22	3.37
7.15	7.88	113.	8	225.28	2048	0.11	5.65
14.3	1.97	56.3	512	450.56	1024	0.44	1.87
28.8	1.96	113.	512	901.12	2048	0.44	1.89

transform of $\dot{u}_{ij}$, and then project the result according to Eq. (31) to find $\dot{h}_{ij}^{\text{TT}}(\mathbf{k}, t)$. From this we then calculate the gravitational wave power spectrum. It should be noted that in our units $G = 1$, though in general we plot quantities that do not depend on G.

We can nucleate bubbles simultaneously at the start of the simulation, or indeed with a nucleation rate throughout its duration. In order to compare with earlier studies using the envelope approximation, we nucleate bubbles with an exponentially increasing nucleation rate, using the algorithm given in Ref. [27]. Then the probability of nucleating a bubble per unit volume and time is given by Eq. (18). The parameters of the simultaneous nucleation runs are listed in Table II, and those of the exponential nucleation runs in Table III. We also perform two constant nucleation runs to check that this type of nucleation is consistent with our other results. The parameters of the constant nucleation runs are given in Table IV.

We also wish to study the gravitational wave power spectrum produced after the bubble collision phase is completed. In order to do this, we can simply turn on the evolution of u_{ij} once the bubbles have finished

TABLE III. Parameters of the exponential nucleation simulations used within this paper.

$R_c M$	γ_*	β/M	$R_* M$	N_b	$L\Delta x M$	L	$\Delta x M$	γ_*^{lat}
7.15	1.97	0.180	28.2	8	56.32	128	0.44	1.85
7.15	1.92	0.180	27.5	69	112.64	256	0.44	1.81
7.15	1.96	0.180	28.0	522	225.28	512	0.44	1.84
7.15	3.94	0.0625	56.3	8	112.64	512	0.22	3.37
7.15	4.09	0.0625	58.5	57	225.28	1024	0.22	3.55
7.15	7.57	0.0290	108.	9	225.28	2048	0.11	5.58

TABLE IV. Parameters of the constant nucleation simulations used within this paper.

$R_c M$	γ_*	p_c/M^4	$R_* M$	N_b	$L\Delta x M$	L	$\Delta x M$	γ_*^{lat}
7.15	3.94	1.50×10^{-7}	56.3	64	225.28	1024	0.22	3.37
7.15	4.09	1.50×10^{-7}	56.3	510	450.56	2048	0.22	3.37

colliding. We employ this approach for a series of simultaneous nucleation simulations listed in Table V.

There are a number of length scales within our simulation. The largest physical length scale within our system is the average separation between bubbles R_*. This is simply given by

$$R_* = \left(\frac{\mathcal{V}}{N_b}\right)^{1/3}. \tag{45}$$

Much smaller than this length scale is the radius of the critical bubble R_c, and the critical bubble wall width l_0. The critical bubble wall width is associated with the scalar field mass in the broken phase. Smaller still is the length scale of the Lorentz contracted bubble walls. We define $\gamma_* = R_*/2R_c$ which is the expected Lorentz factor for a bubble with diameter R_*, and then define $l_* = l_0/\gamma_*$ as the width of the Lorentz contracted bubble wall with a diameter of R_*. It is crucial that we have a good resolution of the bubble walls up until they collide, and as such we need our lattice spacing $\Delta x \ll l_*$. Note that by obtaining different values of R_c we can vary R_* while keeping γ_* the same.

In most vacuum phase transitions we expect bubbles to expand to many times the size of the critical bubble, and therefore up to very high Lorentz factors. We also would like to have many bubbles within our simulation box to obtain an accurate ensemble. Hence, we need sufficiently large lattices to separate the scales

$$\Delta x \ll l_* \ll l_0 \lesssim R_c \ll R_* \ll L\Delta x. \tag{46}$$

It is not possible to perform a simulation in which we achieve a realistic value for γ_* and a correct separation of scales. Instead, we perform multiple simulations with

TABLE V. Parameters of the simultaneous nucleation simulations where the metric perturbations are turned on at $t/R_* = 2.0$ at which point most of the bubbles have finished colliding. This is in order to see the shape of the power spectrum due to scalar field radiation during the oscillation phase.

$R_c M$	γ_*	$R_* M$	N_b	$L\Delta x M$	L	$\Delta x M$	γ_*^{lat}
7.15	3.94	56.3	64	225.28	1024	0.44	3.37
14.3	1.97	56.3	512	450.56	1024	0.44	1.87
14.3	3.94	113.	8	225.28	1024	0.22	3.34
28.8	1.96	113.	64	450.56	1024	0.44	1.89

increasing values of γ_* to attempt to identify a trend as $\gamma_* \to \infty$.

For simulations with a given nucleation rate, we typically expect the first bubble nucleated to grow to a larger size than bubbles nucleated later, and so the wall of the first bubble when it collides will have γ greater than γ_*. Its bubble wall at collision will therefore be thinner than l_*. This effect is particularly pronounced for simulations with an exponential nucleation rate where the first bubble nucleated often grows to be many times larger than the subsequent bubbles at collision time. For a simultaneous nucleation run the diameters of the bubbles will be more closely distributed around R_*, and so the thinnest wall at collision will be much closer to l_*.

For an exponential nucleation rate simulation we need a much finer lattice spacing in comparison to a simultaneous nucleation simulation with the same l_*. In practice, reducing the lattice spacing is too expensive and for large volumes we become unable to trust our results due to bad energy conservation.

V. RESULTS: SCALAR FIELD

As described in the previous section, the scalar field evolution can roughly be split into three stages, expansion, collision, and oscillation. Slices through a simultaneous nucleation simulation volume are shown in Fig. 2. During collision, we see many regions in which the scalar field is
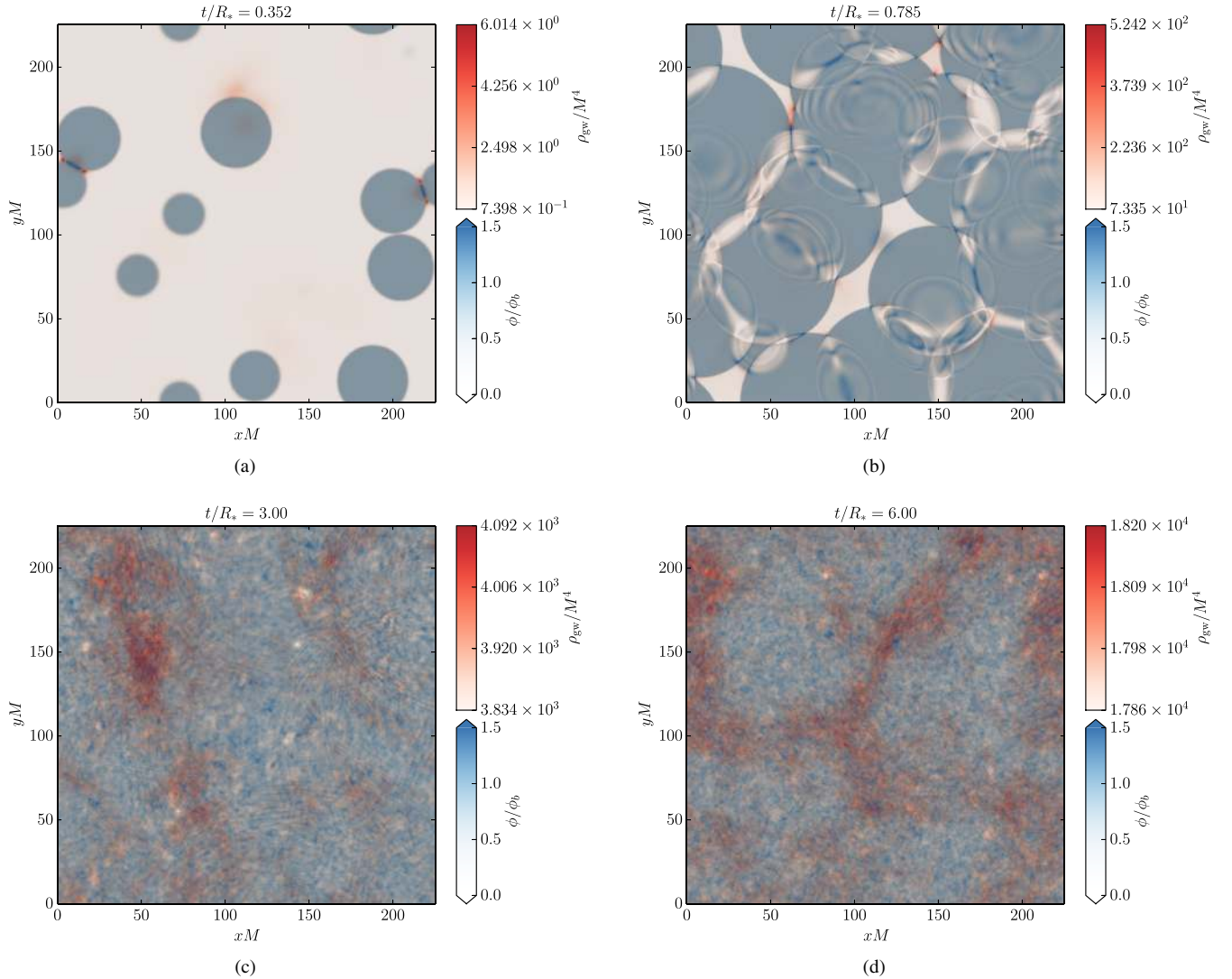
FIG. 2. Slices through a simultaneous nucleation simulation with parameters $R_c M = 7.15$, $N_b = 64$ and $R_* M = 56.32$ showing the expansion (a), collision (b), and oscillatory (c and d) phase of the scalar field. The scalar field value is shown in blue, and the gravitational wave energy density is shown in red. Note that the range of the colorbar for the gravitational wave energy density changes for each plot. During the oscillatory phase the gravitational wave energy density becomes very uniform and the "hotspots" are deviations on the sub percent level. The full set of parameters for this run is shown in Table II. A movie based on this simulation is included in the supplemental material [[40]].
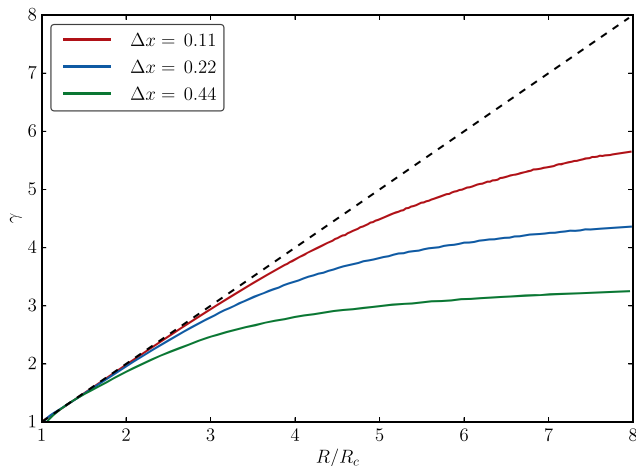
FIG. 3. The Lorentz factor γ of the bubble wall for different values lattice spacings plotted against the radius of the bubble in units of the critical radius. This is for a bubble with $R_c M = 7.15$. The dashed black line shows $\gamma = R/R_c$.
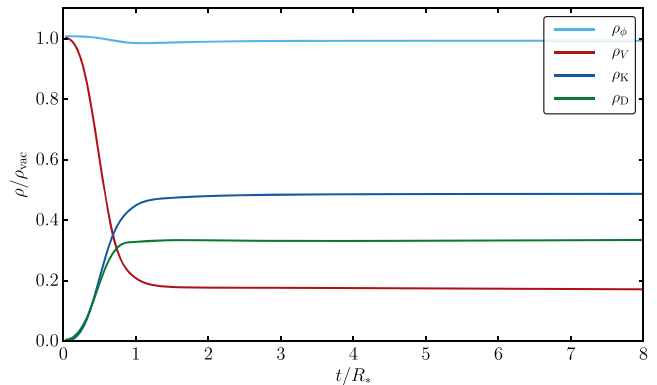

FIG. 4. Energy densities in the scalar field over time for a simultaneous nucleation run with $R_c M = 7.15$, $R_* M = 56.3$ and $N_b = 4096$. The full set of parameters for this run is shown in Table II.

rebounding into the symmetric phase as described in Sec. II D. During the oscillation phase the scalar field becomes more homogeneous on large scales while the scalar field continues to oscillate on small wavelengths. This persists as long as the simulations run, for times that are many multiples of R_*.

In order to test for lattice effects, we study single bubbles, whose Lorentz factors should be related to their radius through Eq. (25). We find the volume by counting the number of lattice sites with $\phi > \phi_b$, and then from this we are able to deduce the bubble radius R and the Lorentz factor of the wall γ.

We plot γ against R in Fig. 3. The lattice effects are easy to see, as γ is highly sensitive to small changes in velocity when $v_w \to 1$. The bubble wall is stopped from contracting beyond a width which is representable on the lattice, and the bubble wall is unable to increase its velocity. The energy that is lost is transferred to small wavelength oscillations that follow behind the bubble wall. This effect has been seen previously in accelerating kinks on a lattice [41,42].

If the deviation of γ from its theoretical value becomes sufficiently large then this can be associated with loss of energy conservation.

We plot the energy densities over time for a simultaneous nucleation phase transition in Fig. 4. As the bubbles expand the potential energy drops steeply and the kinetic and gradient energies increase. Initially, the gradient energy and kinetic energy are roughly equal but when the bubbles begin to collide the kinetic energy becomes larger than the gradient energy. Shortly after the phase transition enters the oscillation stage, with $\rho_V \neq 0$.

The energy conservation for a series of simulations with $L\Delta x = 225.28$ is given in Fig. 5. We can see that energy conservation is substantially better in the simultaneous

nucleations in comparison to the exponential nucleation runs. This is what we expected due to the biggest bubble/ thinnest wall effect mention in Sec. IV. These are the largest volume simulation runs for exponential nucleation, and so have the worst energy violation of all simulations performed. Even in the worst case, energy conservation violation is still kept to $\lesssim 5\%$.

To monitor energy conservation in our multibubble simulations, we define a new parameter γ_*^{lat} which is the numeric value found for γ on the lattice when the bubble radius is $R = R_*$. This new parameter is listed for all simulation runs in their respective tables.

The power spectrum of the scalar field $\mathcal{P}_\phi$ can inform us about the length scales of the shear stresses sourcing gravitational waves. We plot $\mathcal{P}_\phi$ during the expansion, collision and oscillation phases for both a simultaneous and exponential nucleation run in Fig. 6. During expansion and collision $\mathcal{P}_\phi$ is peaked around R_*. During the oscillation
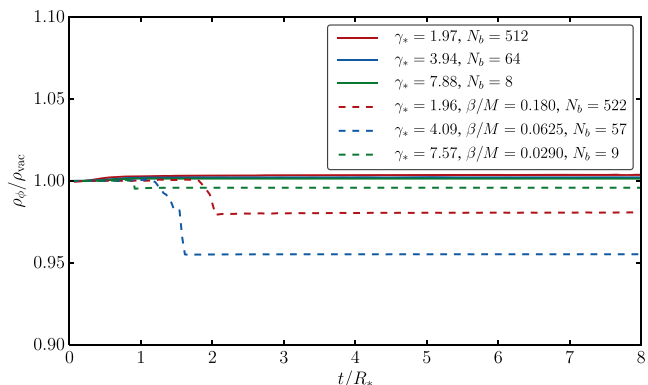

FIG. 5. Energy conservation for several simulations of the same physical volume. Runs with exponential nucleation are plotted with dashed lines, and simultaneous nucleation runs are shown with solid lines. See Tables II and III for the full set of parameters of each run.
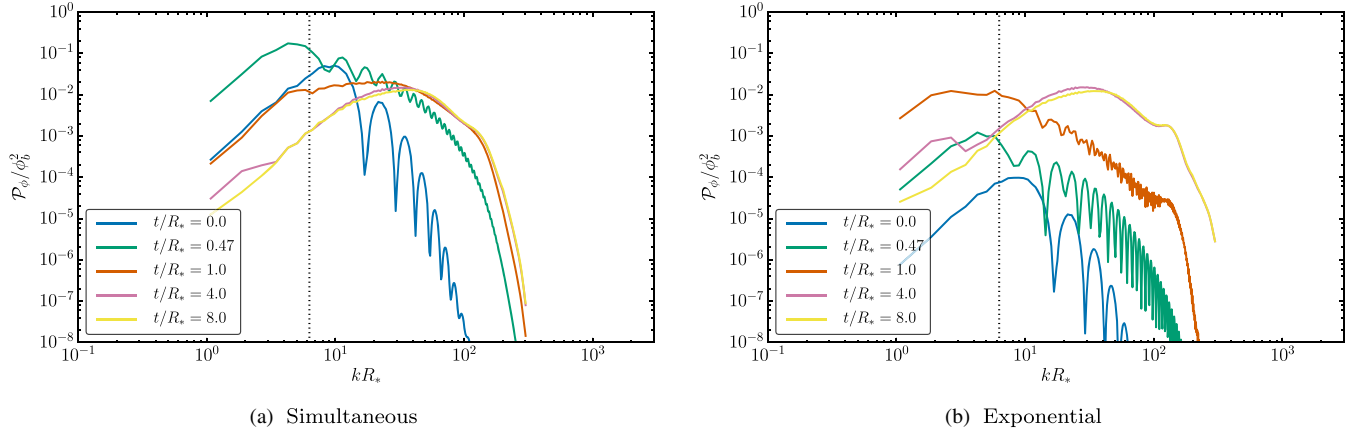
(a) Simultaneous

(b) Exponential

FIG. 6. Scalar power spectra for simultaneous (left) and exponential (right) nucleation runs. Both simulations have $R_c M = 7.15$. The left plot has $N_b = 512$ and $\gamma_* = 1.97$, while the right plot has $N_b = 522$ and $\gamma_* = 1.96$. The full set of parameters of each run can be extracted from Tables II and III. The initial configuration of the scalar field is seen at $t/R_* = 0$. The bubble expansion phase is seen for $t/R_* = 0.47$. The spectrum during bubble collision is seen at $t/R_* = 1.0$. The late time power spectrum after bubbles have collided is then shown at $t/R_* = 4.0$ and $t/R_* = 8.0$. The vertical black dotted line denotes $k = 2\pi/R_*$.

phase $\mathcal{P}_\phi$ shifts so that its maximum is at a higher wavelength, closer to the scale associated with l_0. This can be understood as the structure of bubbles disappearing and being replaced with oscillating features around the mass scale of the scalar field.

The main differences in $\mathcal{P}_\phi$ between the simultaneous and exponential nucleation runs are during the expansion and collision phases. Identical bubbles are all spawned at the start of the simultaneous nucleation run, and so $\mathcal{P}_\phi$ has a larger magnitude at $t/R_* = 0.0$, and shows the characteristic "ringing" of the single-bubble power spectrum. These bubbles then expand in a uniform way, their geometries differentiating from each other only upon collision with another bubble. Comparatively, as more bubbles are spawned during the exponential nucleation run $\mathcal{P}_\phi$ becomes smoother on large scales and noisier on small
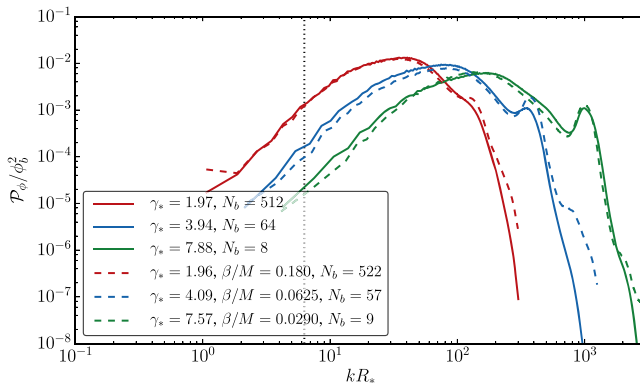

FIG. 7. Comparison of the late time scalar power spectrum at $t/R_* = 8.0$ for both simultaneous (solid lines) and exponential (dashed lines) nucleation runs. All runs use bubbles with $R_c M = 7.15$. See Tables II and III for the full set of parameters of each run.

scales as bubbles of varying sizes appear. The collision phase also lasts longer, and the distribution of bubbles is not as homogeneous as in a simultaneous nucleation run.

If we plot the late time scalar field power spectrum together on the same graph we can clearly see that during the oscillation phase the simultaneous and exponential nucleation runs settle into similar states. We do this for several values of γ_* in Fig. 7. In all cases, the scalar power spectra settle into similar states apart from lattice effects in the UV.

VI. RESULTS: GRAVITATIONAL WAVES

A. Simultaneous nucleation

In Fig. 2, we also show in shades of red the gravitational wave energy density $\rho_{gw}(\mathbf{x}, t)$ sourced by the scalar field. To obtain ρ_{gw} in real space we first perform the Fourier transform of $\dot{u}_{ij}$, then project this to obtain $\dot{h}_{ij}^{TT}$ in k-space. Finally we perform the inverse Fourier transform to find $\dot{h}_{ij}^{TT}$ in real space. From this we then calculate $\rho_{gw}(\mathbf{x}, t)$ using Eq. (29).

We can clearly see from Fig. 2 that during the collision phase hotspots in ρ_{gw} are located in regions where bubbles are colliding. These are the locations where the spherical symmetry of the expanding bubbles is broken. During the oscillation phase the gravitational wave energy density becomes largely homogeneous with fluctuations on the percent level, though gravitational waves continue to be sourced.

In Fig. 8, we plot the gravitational wave power spectrum at several times over the duration of a simultaneous nucleation simulation with $\gamma_* \simeq 4$. As the bubbles begin to collide we begin to see a peak in the spectrum emerging near $k = 2\pi/R_*$, with a power law fall-off towards the UV. For this simulation we do not have a sufficient separation
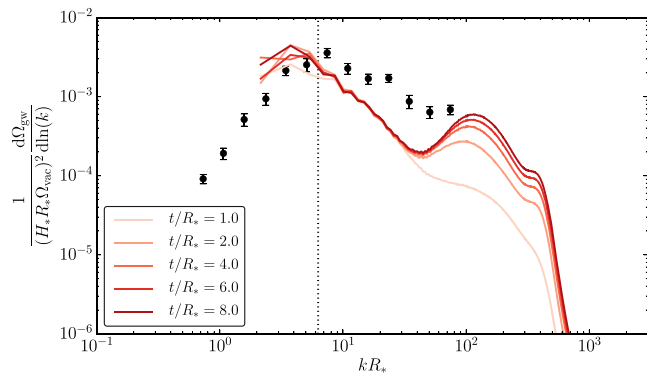
FIG. 8. The gravitational wave power spectrum for the simultaneous nucleation run with $R_cM = 7.15$, $N_b = 64$ and $\gamma_* = 3.94$ listed in Table II. The vertical black dotted line marks where $k = 2\pi/R_*$. The black data points are the results for running a simulation with the envelope approximation with the same bubble locations and nucleation times.
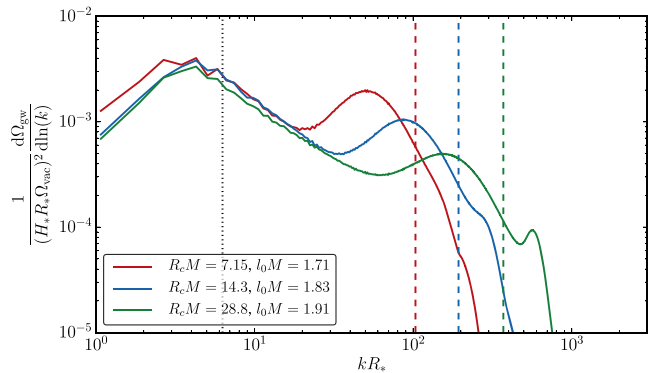

FIG. 9. Gravitational wave power spectrum for several runs with different critical radius R_c and R_*. For each simulation the power spectra have been averaged over the interval $2.5 \leq t/R_* \leq 8.0$. All simulations shown have the same number of bubbles $N_b = 512$ and $\gamma_* \simeq 2$, with the full set of parameters listed in Table II. We also plot the length scale associated with R_* as the vertical black dotted line, and the corresponding length scale for the initial wall width l_0 for each simulation as colored dashed lines.

between R_* and $L\Delta x$ to estimate the power law towards the IR. As the collision phase completes this peak and the power law towards the IR persists, but a second peak associated with a much smaller length scale continues to grow. This second peak is due to gravitational waves sourced from oscillations in the scalar field with wavelengths close to the inverse mass of the scalar field.

In the same figure, we also plot the results of a numerical calculation in the envelope approximation, as detailed in [22], using the same bubble nucleation locations. The peak power in our simulation is closely reproduced by the envelope calculation, although the envelope calculation predicts that the peak is at higher frequency. The power law towards the UV is somewhat steeper in the numerical simulations than in the envelope calculation.

We can show that the frequency of peak power is associated with the length scale of R_*, whereas the bump in the UV is associated with the length scale l_0. In Fig. 9, we plot the power spectra for three runs with different values of R_c and R_* but the same γ_*. It can be seen that the power peaks at $kR_* \simeq 3$, with a secondary peak at $kl_0 \simeq 3$.

In a realistic transition, the separation between R_* and l_0 will be many orders of magnitude, and we would expect the UV peak will be greatly suppressed due to the fall-off of the power spectrum with increasing k. We will estimate how large it can grow below.

Note that the power spectrum fluctuates due to the oscillations in the individual Fourier modes. In order to minimize this effect, in some plots we average over power spectra produced during an interval spanning several t/R_*. On these occasions the details are given in the caption of the figure.

We show the runs with $R_cM = 7.15$ from Table II in Fig. 10. By increasing N_b while keeping R_* the same we are able to see further into the IR for a given γ_*. Apart from this increasing, N_b does not have a significant effect on the

shape of the power spectrum, implying that $N_b = 8$ is sufficient to measure the slope of the power law towards the UV. Increasing γ_* does not change the location or amplitude of the IR peak in respect to R_*. While the slope of the power spectrum towards the IR is in agreement with k^{-1} for $\gamma_* \simeq 2$, it appears steeper for $\gamma_* \simeq 4$ and $\gamma_* \simeq 8$. Between $\gamma_* \simeq 4$ and $\gamma_* \simeq 8$ the slope appears consistent.

B. Exponential and constant nucleation

In Fig. 11, we show the evolution of the power spectra for an exponential nucleation run with $\gamma_* \simeq 4$. Similar to in Fig. 8 we plot the results of a simulation using the envelope approximation as detailed in [22] using the same bubble nucleation locations and times.
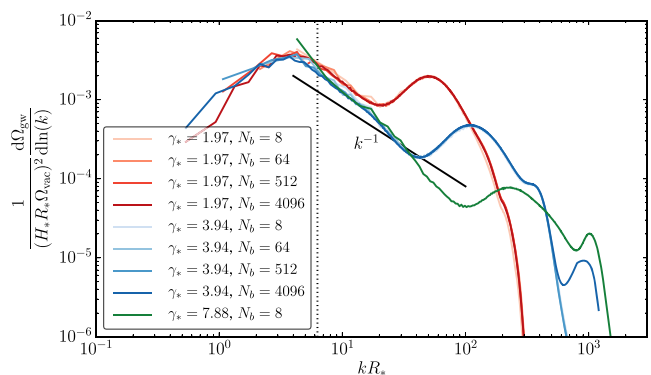

FIG. 10. Gravitational wave power spectrum for all simultaneous bubble runs with $R_cM = 7.15$. The parameters for these runs are given in Table II. For each simulation the power spectra have been averaged over the interval $2.5 \leq t/R_* \leq 8.0$. The solid black line shows a power law of k^{-1}. We plot as a vertical black dotted line the wave number $k = 2\pi/R_*$. See Table II for the full set of parameters of each run.
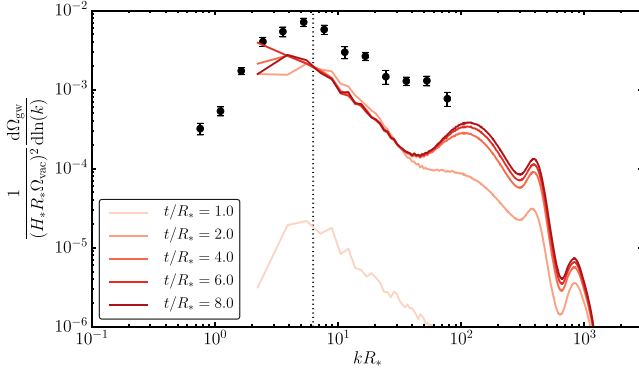
FIG. 11. Gravitational wave power spectrum for the exponential nucleation run with $R_c M = 7.15$, $N_b = 57$ and $\gamma_* = 4.09$ listed in Table II. The vertical black dotted line marks where $k = 2\pi/R_*$. The black data points are the results for running a simulation with the envelope approximation with the same bubble locations and nucleation times.

For the exponential nucleation run we see that the envelope simulation gives an overestimate of peak amplitude, but is still within an order of magnitude. From the full scalar field simulation we obtain a similar peak amplitude as in the simultaneous nucleation run shown in Fig. 8. This indicates that the scaling of gravitational wave production for our simulations is governed by R_* rather than β. Once again the peak location is shifted slightly into the IR in comparison to the envelope simulation.

The power spectra for all exponential simulation runs are shown in Fig. 12. For similar γ_*, we see convergence to the resulting slope of the power spectra for even small numbers of bubbles, implying that even $N_b = 8$ creates a satisfactory ensemble.

All simulations seem to be consistent regarding the location and height of the peak in the IR and there is even agreement with the simultaneous nucleation runs. The

slope of the power spectrum towards the IR is steeper than k^{-1} for $\gamma_* \simeq 4$ and $\gamma_* \simeq 8$, and appears consistent between them.

The two constant nucleation runs listed in Table IV are found to produce power spectra that are consistent with the simultaneous and exponential nucleation runs. We plot the power spectra for the constant nucleation runs along with the other $\gamma_* \simeq 4$ runs in Fig. 15.

C. Late time power spectrum

We are able to see the shape of the power spectrum generated during the oscillation phase by setting $u_{ij} = 0$ after the collision phase has completed. We chose a time $t/R_* = 2$ to set $u_{ij} = 0$. However for some simulations there appears to have been regions in which bubbles were still colliding at this time, and so a later time should have been chosen. For these simulations there is an uptick in the power spectrum in the IR, which can contribute significantly to the energy density. As the IR bins consist of only a few modes, there can be large oscillations in Ω_{gw}.

The evolution of the power spectrum from the oscillation phase is shown in Fig. 13. The spectrum consists of a bump in the UV corresponding to the length scale of l_0 and also a plateau extending from the bump up to just before the length scale of R_* in the IR. A similar shape can perhaps be discerned in Ref. [25], where the contribution to the total power spectrum from the oscillation phase appears to dominate. In the aforementioned study, the gravitational power spectrum from collisions was estimated to be between 2 and 3 orders of magnitude smaller than that predicted by the envelope approximation. The reason for this deficit is unclear. There was also a relatively small scale separation between R_* and l_0, as γ_* ranges between $\gamma_* \simeq 2$ and $\gamma_* \simeq 3$. Together these may explain why the
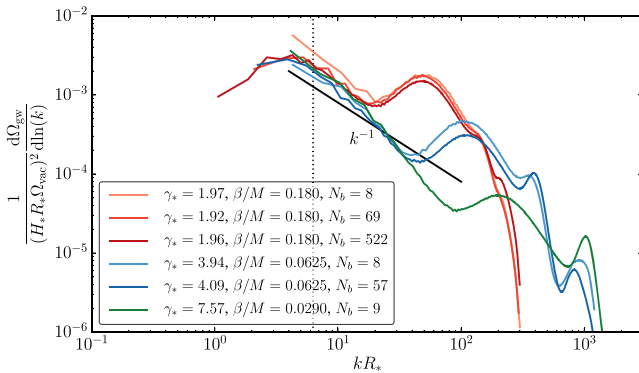

FIG. 12. Gravitational wave power spectrum for all exponential nucleation runs with $R_c M = 7.15$. The parameters for these runs are given in Table III. For each simulation the power spectra have been averaged over the interval $2.5 \leq t/R_* \leq 8.0$. The solid black line shows a power law of k^{-1}. Also plotted as a vertical black dotted line is $kR_* = 2\pi$.
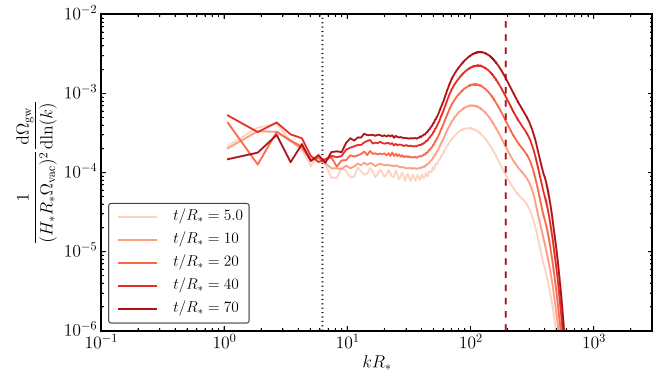

FIG. 13. Late time power spectrum from gravitational waves generated from the oscillation stage. Metric perturbations are only turned on after $t/R_* = 2$. This is for the run with $R_c M = 14.3$, $N_b = 512$ and $\gamma_* = 3.94$ listed in Table V, where the full set of parameters of this run are given. The vertical black dotted line designates where $k = 2\pi/R_*$ and the dashed red line shows where $k = 2\pi/l_0$.
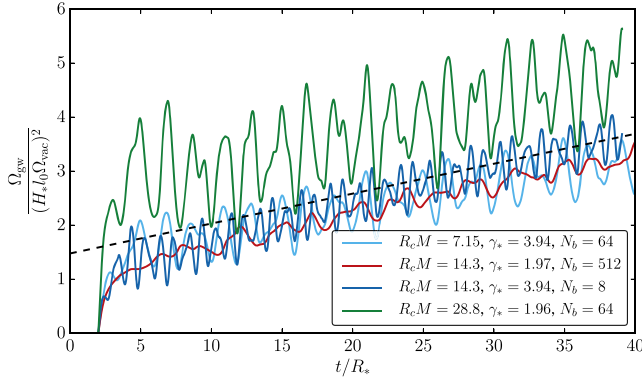
FIG. 14.　Total $\Omega_{\rm gw}$ from gravitational waves generated after $t/R_* = 2$ for a series of simulations with different R_c, N_b and γ_*, see Table V. The oscillations are due to ringing in the IR of the power spectrum. The dashed black line is a fit for the rate of increase of $\Omega_{\rm gw}$, with a slope of $d\Omega_{\rm gw}/dt = 0.06(H_*l_0\Omega_{\rm vac})^2/R_*$.
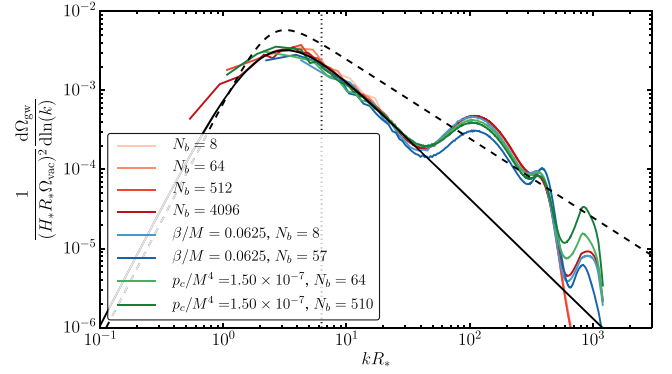

FIG. 15.　Scaled gravitational wave power spectrum for all simulations with $\gamma_* \simeq 4$. For each simulation the power spectra have been averaged over the interval $2.5 \leq t/R_* \leq 8.0$. Simultaneous nucleation runs are plotted in red, exponential nucleation in blue, and constant nucleation in green. From these simulation runs we make a fit for the gravitational wave power spectrum from bubble collisions given R_*, which is shown as the black solid line. The envelope approximation fit as given in [16] is shown as the dashed black line, where we have used Eq. (56) to convert between β and R_*.

contribution from the oscillation phase dominated that of bubble collisions.

We can see that the power spectrum continues to grow during the oscillation phase. One might conclude that the contribution from the oscillation phase would eventually dominate that from the bubble collisions. We therefore plot $\Omega_{\rm gw}$ for a set of simulations where the metric perturbations are turned on after $t/R_* = 2.0$ in Fig. 14. We are able to estimate the growth of $\Omega_{\rm gw}$ during the oscillation phase from these simulations. We find that

$$\frac{d\Omega_{\rm gw}^{\rm osc}}{dt} \sim 10^{-1} \frac{(H_*l_0\Omega_{\rm vac})^2}{R_*}. \qquad (47)$$

The largest amount of time that $\Omega_{\rm gw}^{\rm osc}$ can grow before the growth is cut off by expansion [19] is one Hubble time H_*^{-1}.

From our earlier plots we can estimate the contribution to $\Omega_{\rm gw}$ from the bubble collision phase is

$$\Omega_{\rm gw}^{\rm coll} \sim 10^{-3}(H_*R_*\Omega_{\rm vac})^2. \qquad (48)$$

Therefore the ratio between these two contributions is

$$\frac{\Omega_{\rm gw}^{\rm coll}}{\Omega_{\rm gw}^{\rm osc}} \sim 10^{-2}(R_*H_*)^3 \frac{1}{(l_0H_*)^2}, \qquad (49)$$

$$\sim 10^{-3} \frac{H_*^3}{n_b} \frac{(M_b m_{\rm Pl})^2}{\rho_c}, \qquad (50)$$

where $m_{\rm pl}$ is the Planck mass. For a vacuum dominated phase transition $\rho_c \sim \rho_{\rm vac} < \frac{1}{12\lambda} M_b^4$.

$$\frac{\Omega_{\rm gw}^{\rm coll}}{\Omega_{\rm gw}^{\rm osc}} \gtrsim 10^{-1} \frac{H_*^3}{n_b} \left(\frac{m_{\rm Pl}}{M_b}\right)^2. \qquad (51)$$

Providing that the mass scale of the phase transition is sufficiently smaller than the Planck scale, the contribution from the collision phase should dominate.

D. Fitting

In Fig. 15, we plot gravitational wave power spectra from all simultaneous, exponential and constant nucleation runs with $\gamma_* \simeq 4$. We can see that they seem to be consistent, indicating that nucleation rate makes little difference to the power spectra as a function of kR_*. We can therefore provide a fit for the gravitational wave power spectrum from collisions, applying to all nucleation histories.

The first two bins of the numerical power spectra contain very few modes and are expected to be significantly affected by finite size effects. To produce our fit we shall use the largest simultaneous nucleation simulation for $\gamma_* \simeq 4$ with $N_b = 4096$ as this provides us with the largest dynamic range. This is the only simulation in which we can resolve the peak location after removing the first two bins.

Even so, we do not have sufficient dynamic range to be able to estimate the power law towards the IR. On causal grounds, though, it is expected that the IR power goes as k^3 [37]. Our peak is somewhat broader than previously seen in the envelope approximation.

We find a fit of the following form

$$\frac{d\Omega_{\rm gw}^{\rm fit}}{d\ln k} = \Omega_{\rm p}^{\rm fit} \frac{(a+b)^c \tilde{k}^b k^a}{(b\tilde{k}^{(a+b)/c} + ak^{(a+b)/c})^c}, \qquad (52)$$

where we fix $a = 3$. Then we find that

$$\Omega_{\rm p}^{\rm fit} = (3.22 \pm 0.04) \times 10^{-3}(H_*R_*\Omega_{\rm vac})^2, \qquad (53)$$

$$\tilde{k}R_* = 3.20 \pm 0.04, \qquad (54)$$

$$b = 1.51 \pm 0.04, \qquad c = 2.18 \pm 0.15, \qquad (55)$$

with errors taken from the covariance matrix of the fit. We plot our fit in Fig. 15.

We provide the fit in terms of the mean bubble separation R_*, which has a clear definition in all nucleation histories, and is related to the nucleation probability through equations (21), (19) and (23), and the definition of $R_* = n_b^{-1/3}$. For example, for exponential nucleation,

$$\beta = \frac{(8\pi)^{1/3} v_w}{R_*}. \tag{56}$$

Using Eq. (56) with $v_w = 0.97$ we find that

$$\frac{\Omega_p^{fit}}{\Omega_p^{env}} = 0.55, \tag{57}$$

and

$$\frac{\tilde{k}_{fit}}{\tilde{k}_{env}} = 1.0. \tag{58}$$

We plot both our fit and also the fit from the envelope approximation in Fig. 15.

VII. CONCLUSIONS

We have performed the largest scale lattice simulations of a pure vacuum transition to date. In doing so, we have been able to test the envelope approximation's description of the resulting gravitational wave power spectrum, at high bubble wall Lorentz factors γ_* and for many bubbles. We have simulated three different bubble nucleation histories, where bubbles are either nucleated simultaneously, with an exponentially increasing nucleation rate, or with a constant rate.

In our simulations, the peak gravitational wave power has approximate agreement with the most recent envelope approximation fit [16], to within a factor of two. The peak frequency in the envelope approximation fit has very good agreement with our results.

When the gravitational wave power is calculated using the envelope approximation's model of the actual bubbles of our simulation, the peak location is shifted towards slightly higher frequencies.

As we increase γ_* beyond $\gamma_* \simeq 2$ we find that the power law on the high frequency side of the peak becomes approximately $k^{-1.5}$, steeper than the k^{-1} predicted by the envelope approximation.[1] The power law on the low

frequency side is consistent with the k^3 predicted by causality [37,43], but we do not have sufficient dynamic range for an independent estimate. We provide a 3-parameter fit to our results Eq. (52).

In our simulations, the overlap regions where bubbles have recently collided have extended regions in which the scalar field has large amplitude oscillations around the true vacuum, even returning to the false vacuum. These regions are not accounted for in the envelope approximation, and may be a source of its inaccuracy. Large amplitude nonlinear oscillations with wavelength of order the bubble wall width l_0 continue long after the bubbles finish colliding, which is also not included in the envelope approximation. These oscillations source gravitational waves which lead to an additional bump in the UV of the power spectrum at a frequency of order l_0^{-1}.

In the early Universe, the gravitational wave source will eventually diminish due to thermalization and Hubble expansion. We find that even if the bump continues to grow for as long as a Hubble time, H_*^{-1}, the power spectrum from the oscillation phase will be subdominant to that of bubble collisions providing that the mass of the scalar field is much less than the Planck mass.

In testing the envelope approximation and investigating the oscillatory phase of the scalar field, we have neglected the expansion of the Universe, and therefore the fit we provide strictly applies only to transitions in which the duration is much shorter than the Hubble time H_*^{-1}. There is more work to do to study the case where the Universe enters an inflationary phase before bubbles start nucleating.

---

[1]This steeper power law is closer to the $k^{-1.8}$ reported for two-bubble collisions [12,13], widely taken to be the envelope approximation prediction before the work of Ref. [15].

[1] B. P. Abbott *et al.* (Virgo, LIGO Scientific Collaborations), Phys. Rev. Lett. **116**, 241103 (2016).

[2] B. P. Abbott *et al.* (Virgo, LIGO Scientific Collaborations), Phys. Rev. Lett. **116**, 061102 (2016).

[3] H. Audley *et al.*, arXiv:1702.00786.

[4] C. Caprini and D. G. Figueroa, arXiv:1801.04268.

[5] C. Caprini *et al.*, J. Cosmol. Astropart. Phys. 04 (2016) 001.

[6] D. J. Weir, in Phil. Trans. R. Soc. A **2018**, 376 (2017).

[7] S. R. Coleman, Phys. Rev. D **15**, 2929 (1977); **16**, 1248(E) (1977).

[8] A. D. Linde, Nucl. Phys. **B216**, 421 (1983); **B223**, 544(E) (1983).

[9] P. J. Steinhardt, Phys. Rev. D **25**, 2074 (1982).

[10] E. Witten, Phys. Rev. D **30**, 272 (1984).

[11] C. J. Hogan, Mon. Not. R. Astron. Soc. **218**, 629 (1986).

[12] A. Kosowsky, M. S. Turner, and R. Watkins, Phys. Rev. D **45**, 4514 (1992).

[13] A. Kosowsky and M. S. Turner, Phys. Rev. D **47**, 4372 (1993).

[14] M. Kamionkowski, A. Kosowsky, and M. S. Turner, Phys. Rev. D **49**, 2837 (1994).

[15] S. J. Huber and T. Konstandin, J. Cosmol. Astropart. Phys. 09 (2008) 022.

[16] T. Konstandin, J. Cosmol. Astropart. Phys. 03 (2018) 047.

[17] C. Caprini, R. Durrer, and G. Servant, Phys. Rev. D **77**, 124015 (2008).

[18] M. Hindmarsh, S. J. Huber, K. Rummukainen, and D. J. Weir, Phys. Rev. Lett. **112**, 041301 (2014).

[19] M. Hindmarsh, S. J. Huber, K. Rummukainen, and D. J. Weir, Phys. Rev. D **92**, 123009 (2015).

[20] M. Hindmarsh, S. J. Huber, K. Rummukainen, and D. J. Weir, Phys. Rev. D **96**, 103520 (2017).

[21] M. Hindmarsh, Phys. Rev. Lett. **120**, 071301 (2018).

[22] D. J. Weir, Phys. Rev. D **93**, 124037 (2016).

[23] R. Jinno and M. Takimoto, Phys. Rev. D **95**, 024009 (2017).

[24] R. Jinno and M. Takimoto, arXiv:1707.03111.

[25] H. L. Child and J. T. Giblin, Jr., J. Cosmol. Astropart. Phys. 10 (2012) 001.

[26] A. Kosowsky and M. S. Turner, Phys. Rev. D **47**, 4372 (1993).

[27] K. Enqvist, J. Ignatius, K. Kajantie, and K. Rummukainen, Phys. Rev. D **45**, 3415 (1992).

[28] R. Jinno, S. Lee, H. Seong, and M. Takimoto, J. Cosmol. Astropart. Phys. 11 (2017) 050.

[29] I. Garcia Garcia, S. Krippendorf, and J. March-Russell, Phys. Lett. B **779**, 348 (2018).

[30] S. W. Hawking, I. G. Moss, and J. M. Stewart, Phys. Rev. D **26**, 2681 (1982).

[31] J. Braden, J. R. Bond, and L. Mersini-Houghton, J. Cosmol. Astropart. Phys. 03 (2015) 007.

[32] J. Zhang and Y.-S. Piao, Phys. Rev. D **82**, 043507 (2010).

[33] G. Aarts, G. F. Bonini, and C. Wetterich, Nucl. Phys. **B587**, 403 (2000).

[34] R. Micha and I. I. Tkachev, Phys. Rev. Lett. **90**, 121301 (2003).

[35] A. Arrizabalaga, J. Smit, and A. Tranberg, Phys. Rev. D **72**, 025014 (2005).

[36] J. Garcia-Bellido, D. G. Figueroa, and A. Sastre, Phys. Rev. D **77**, 043517 (2008).

[37] C. Caprini, R. Durrer, T. Konstandin, and G. Servant, Phys. Rev. D **79**, 083519 (2009).

[38] J. F. Dufaux, A. Bergman, G. N. Felder, L. Kofman, and J.-P. Uzan, Phys. Rev. D **76**, 123517 (2007).

[39] D. Daverio, M. Hindmarsh, and N. Bevis, arXiv:1508.05610.

[40] See Supplemental Material at http://link.aps.org/supplemental/10.1103/PhysRevD.97.123513, for a movie showing the scalar field evolution and gravitational wave energy density for a slice through one of our simulations.

[41] J. A. Combs and S. Yip, Phys. Rev. B **28**, 6873 (1983).

[42] M. Peyrard and M. D. Kruskal, Physica **14D**, 88 (1984).

[43] R. Durrer and C. Caprini, J. Cosmol. Astropart. Phys. 11 (2003) 010.